Dirac *R*-matrix calculations of electron-impact excitation of neon-like krypton

D C Griffin[1], C P Ballance[1], D M Mitnik[2] and J C Berengut[3]

[1] Department of Physics, Rollins College, Winter Park, FL 32789, USA
[2] Instituto de Astronomía y Física del Espacio, and Departamento de Física, Universidad de Buenos Aires, Argentina
[3] School of Physics, University of New South Wales, Sydney 2052, Australia

Abstract
We have employed the Dirac *R*-matrix method to determine electron-impact excitation cross sections and effective collision strengths in Ne-like Kr^{26+}. Both the configuration-interaction expansion of the target and the close-coupling expansion employed in the scattering calculation included 139 levels up through $n = 5$. Many of the cross sections are found to exhibit very strong resonances, yet the effects of radiation damping on the resonance contributions are relatively small. Using these collisional data along with multi-configuration Dirac–Fock radiative rates, we have performed collisional-radiative modeling calculations to determine line-intensity ratios for various radiative transitions that have been employed for diagnostics of other Ne-like ions.

(Some figures in this article are in colour only in the electronic version)

1. Introduction

Neon-like ions play an important role in the diagnostics of a wide variety of laboratory and astrophysical plasmas. Primarily because of its importance to astrophysical plasmas, one of the most thoroughly studied neon-like ions is Fe^{16+}. For this ion, there has been a long series of distorted-wave (DW) calculations that include the effects of resonant recombination followed by autoionization [1–4] as well as Breit–Pauli (BP) *R*-matrix [5, 6] and Dirac *R*-matrix [7, 8] calculations of electron-impact excitation. Neon-like krypton is also important, especially as a diagnostic for tokamak plasmas [9]. Although there was some early work on electron-impact excitation of Kr^{26+} using the DW [10], the relativistic DW [11] and Coulomb–Born [12] approximations, the only published *R*-matrix calculation is a 27-level BP calculation by Gupta *et al* [13]. In addition, Rice *et al* [9] carried out extensive calculations of the energy levels, radiative rates and electron-impact cross sections for Ne-like krypton, zirconium, niobium and molybdenum. They employed these data for calculating theoretical spectra and compared them with observed spectra from tokamak plasmas.

Their excitation cross sections were determined in the relativistic DW approximation; however, it is not clear that the contributions from resonant recombination followed by autoionization were included. These contributions are always present in *R*-matrix calculations.

In this paper, we report on the results of a 139-level Dirac *R*-matrix calculation of electron-impact excitation in Kr^{26+}. With resonant contributions to excitation, certain types of radiative rates from recombination resonances increase with ionization stage, while autoionizing rates remain relatively constant. Radiative decay of these resonant states to the bound states of the recombined atom, which is referred to as radiative damping, can reduce the size of these resonances. We have investigated these effects in Kr^{26+} by performing two *R*-matrix calculations—one with radiative damping and one without. By comparing the two results, we are able to assess the importance of damping on the electron-impact excitation of this ion. Finally, we incorporated our calculated radiative and collisional rates in collisional-radiative calculations of line-intensity ratios for a set of transitions that have been employed in the diagnostics of plasmas for other neon-like ions.

The remainder of this paper is organized as follows. In the next section, we describe the calculation of the target wavefunctions and present results for energy levels and oscillator strengths. In section 3, we describe the scattering calculations and present results for excitation cross sections and effective collision strengths as well as line-intensity ratios calculated from these collisional and radiative data. Finally, in section 4, we summarize our findings.

2. The target structure

The target orbitals, energy levels, radiative rates and oscillator strengths for this study were generated using the multi-configuration Dirac–Fock (MCDF) atomic structure program GRASP0 [14, 15]. We included all 139 levels arising from the configurations $2s^2 2p^5 nl$ with $n \leqslant 5$ and $2s2p^6 nl$ with $n \leqslant 4$ in both the configuration-interaction (CI) expansion of the target and the close-coupling (CC) expansion of the subsequent scattering calculations. The theoretical energies from this calculation are given in table 1 in comparison to existing experimental values. We also show the percentage differences between experiment and theory; the average difference for the 38 levels for which there are experimental values is only 0.059%.

In table 2, we present weighted oscillator strengths (gf) calculated in the length gauge for all dipole-allowed transitions to the ground level. We also give the ratios of the length to velocity oscillator strengths and compare the present gf values with those determined by Rice *et al* [9]. The oscillator strength ratios are relatively close to one except for the transitions from the two $2s^2 2p^5 5s$ levels. In addition, with just a few exceptions, the present gf values are in good agreement with those from Rice *et al* [9]. Six transitions in Ne-like ions are used extensively for diagnostics of laboratory and astrophysical plasmas. The theoretical and experimental wavelengths and theoretical radiative rates for these six transitions in Kr^{26+}, along with their standard labels, are given in table 3.

Recently, there has been an ongoing controversy over the effects of electron correlation on the radiative rates and the electron-impact excitation collision strengths associated with the 3C and 3D transitions in Fe^{16+}. For example, Chen [4, 8] states that by adding the two-electron promotion from the 2p to 3d subshell along with a set of pseudostates to a comparable 139-level calculation in Fe^{16+}, he obtained a radiative rate for the 3C transition that is reduced by 9% while the 3D radiative rate is increased by 4%. In addition, he states that these same correlations bring the electron-impact excitation collision strengths into closer agreement with experimental measurements.

We would have liked to determine whether these same correlations would have similar effects in the present Kr^{26+} calculation; however, since Chen [4, 8] does not explain how these pseudostates were generated or what types of correlations they represent, this was not possible. In an earlier study by Dong *et al* [16], the MCDF method was used to perform a systematic study of the effects of electron correlation on the 3C and 3D transitions in the Ne-like ions Cr^{14+}, Fe^{16+}, Ni^{18+}, Zn^{20+}, Ge^{22+}, Se^{24+} and Kr^{26+}. They first included all possible one- and two-electron promotions out of the 2s and 2p subshells of the $1s^2 2s^2 2p^6$ ground configuration to the $3l$, $4l$ and $5l$ subshells that produce levels with even parity and $J = 0$. They then added all possible one- and two-electron promotions out of the 2s, 2p and 3d subshells of the $1s^2 2s^2 2p^5 3d$ excited configuration to the $3l$, $4l$ and $5l$ subshells that produce levels with odd parity and $J = 1$. Applying these two CI expansions to Fe^{16+}, they obtained a weighted oscillator strength for the 3C transition of 2.33, which is 6.4% lower than that from a 139-level calculation [7] without these correlations. For the 3D transition, they obtained a value of 0.675, which is 5.6% higher than that from the same 139-level calculation [7]. For Kr^{26+}, their weighted oscillator strength for the 3C transition was 1.84, which is 4.7% lower than the value given in table 2 for this transition, and for the 3D transition, their weighted oscillator strength was 1.56, only 0.6% higher than the value for this transition given in table 2.

In order to provide an independent test of these results, we have performed CI calculations on the 3C and 3D radiative transitions in both Fe^{16+} and Kr^{26+} using a program that has been employed previously to calculate energy levels, relativistic shifts and isotope shifts in a variety of atoms [17–19]. First, we solved the Dirac–Fock equations for the $1s^2 2s^2 2p^6$ ground configuration. Then we generated valence and virtual orbitals by diagonalizing the Dirac–Fock operator on a basis set of B-splines and selecting the orbitals of lowest energy. The CI calculation was carried out using all orbitals up to $7l$ with $l = $ s, p, d and f, which enabled us to reach a converged result. For our final calculations, we allowed all single and double promotions out of both the 2s and 2p subshells to all valence and virtual orbitals to form states of both even and odd parity. In Fe^{16+} we tested the effects of allowing excitations from the 1s orbital as well, but they were found to make no difference to the accuracy of the radiative rates quoted here. We also investigated the effects of allowing triple promotions up to the $4l$ subshells, but again they were found to be very small. From these calculations for Fe^{16+}, we obtained a 3C weighted oscillator strength of 2.31, and a 3D weighted oscillator strength of 0.66; these values are 0.9% and 2.2% lower, respectively, than those obtained by Dong *et al*. For Kr^{26+} we obtained a 3C weighted oscillator strength of 1.85 and a 3D oscillator strength of 1.53; these are 0.5% higher and 1.9% lower, respectively, than the values obtained by Dong *et al* [16] and 4.1% lower and 1.3% higher, respectively, than the values given in table 2.

Thus, from the earlier work of Dong *et al* [16] and our own large CI calculations, we would expect that these correlations, which are not included in the target states for the scattering calculation, would have relatively small effects on both the radiative rates and the collision strengths reported here.

3. Scattering calculations

The scattering calculations were performed using our suite of parallel Dirac *R*-matrix programs [20] which includes modified portions of the DARC programs [21, 22] as well as a set of modified programs from our parallel BP *R*-matrix

Table 1. Energies in rydbergs for the first 139 levels in Kr^{26+} relative to the 2p^6 ^{1}S$_0$ ground level.

No.	Conf.	Level (j–j)	Purity	MCDF[a] energy	Exp.[b] energy	% Diff.
1	2s^{2}2p^6	^{1}S$_0$	0.999	0.000	0.000	0.000
2	2s^{2}2p^{5}3s	(3/2,1/2)$_2$	0.999	121.192	121.204	+0.010
3	2s^{2}2p^{5}3s	(3/2,1/2)$_1$	0.998	121.426	121.441	+0.013
4	2s^{2}2p^{5}3p	(3/2,1/2)$_1$	0.952	124.964	124.966	+0.001
5	2s^{2}2p^{5}3p	(3/2,1/2)$_2$	0.999	125.200	125.194	−0.005
6	2s^{2}2p^{5}3s	(1/2,1/2)$_0$	0.999	125.303	125.284	−0.015
7	2s^{2}2p^{5}3s	(1/2,1/2)$_1$	0.998	125.430	125.400	−0.025
8	2s^{2}2p^{5}3p	(3/2,3/2)$_3$	1.000	126.072	126.041	−0.024
9	2s^{2}2p^{5}3p	(3/2,3/2)$_1$	0.951	126.100	126.084	−0.013
10	2s^{2}2p^{5}3p	(3/2,3/2)$_2$	1.000	126.410	126.397	−0.010
11	2s^{2}2p^{5}3p	(3/2,3/2)$_0$	0.917	127.588	127.618	+0.024
12	2s^{2}2p^{5}3p	(1/2,1/2)$_1$	0.997	129.225	129.175	−0.039
13	2s^{2}2p^{5}3p	(1/2,3/2)$_1$	0.993	130.241	130.192	−0.038
14	2s^{2}2p^{5}3p	(1/2,3/2)$_2$	0.999	130.347	130.280	−0.051
15	2s^{2}2p^{5}3d	(3/2,3/2)$_0$	0.998	130.745	130.694	−0.039
16	2s^{2}2p^{5}3p	(1/2,1/2)$_0$	0.917	130.908	130.742	−0.127
17	2s^{2}2p^{5}3d	(3/2,3/2)$_1$	0.906	130.936	130.945	+0.008
18	2s^{2}2p^{5}3d	(3/2,3/2)$_3$	0.998	131.232	131.173	−0.045
19	2s^{2}2p^{5}3d	(3/2,5/2)$_2$	0.704	131.266	131.233	−0.025
20	2s^{2}2p^{5}3d	(3/2,5/2)$_4$	1.000	131.274	131.214	−0.045
21	2s^{2}2p^{5}3d	(3/2,3/2)$_2$	0.708	131.496	131.445	−0.039
22	2s^{2}2p^{5}3d	(3/2,5/2)$_3$	0.999	131.723	131.664	−0.046
23	2s^{2}2p^{5}3d	(3/2,5/2)$_1$	0.879	132.551	132.476	−0.057
24	2s^{2}2p^{5}3d	(1/2,3/2)$_2$	0.998	135.304	135.260	−0.032
25	2s^{2}2p^{5}3d	(1/2,5/2)$_2$	0.994	135.522	135.426	−0.071
26	2s^{2}2p^{5}3d	(1/2,5/2)$_3$	0.999	135.640	135.531	−0.081
27	2s^{2}2p^{5}3d	(1/2,3/2)$_1$	0.971	136.226	136.065	−0.118
28	2s2p^{6}3s	(1/2,1/2)$_1$	0.994	139.030		
29	2s2p^{6}3s	(1/2,1/2)$_0$	0.999	139.808		
30	2s2p^{6}3p	(1/2,1/2)$_0$	0.997	142.923		
31	2s2p^{6}3p	(1/2,1/2)$_1$	0.990	143.005		
32	2s2p^{6}3p	(1/2,3/2)$_2$	0.997	143.939		
33	2s2p^{6}3p	(1/2,3/2)$_1$	0.991	144.137	143.835	−0.209
34	2s2p^{6}3d	(1/2,3/2)$_1$	0.999	148.814		
35	2s2p^{6}3d	(1/2,3/2)$_2$	0.856	148.884		
36	2s2p^{6}3d	(1/2,5/2)$_3$	0.999	149.027		
37	2s2p^{6}3d	(1/2,5/2)$_2$	0.856	149.623	149.295	−0.220
38	2s^{2}2p^{5}4s	(3/2,1/2)$_2$	1.000	164.361		
39	2s^{2}2p^{5}4s	(3/2,1/2)$_1$	0.999	164.439	164.388	−0.031
40	2s^{2}2p^{5}4p	(3/2,1/2)$_1$	0.971	165.929		
41	2s^{2}2p^{5}4p	(3/2,1/2)$_2$	1.000	165.992		
42	2s^{2}2p^{5}4p	(3/2,1/2)$_3$	1.000	166.350		
43	2s^{2}2p^{5}4p	(3/2,3/2)$_1$	0.971	166.367		
44	2s^{2}2p^{5}4p	(3/2,3/2)$_2$	1.000	166.469		
45	2s^{2}2p^{5}4p	(3/2,3/2)$_0$	0.992	166.996		
46	2s^{2}2p^{5}4d	(3/2,3/2)$_0$	0.997	168.116		
47	2s^{2}2p^{5}4d	(3/2,3/2)$_1$	0.916	168.190	168.120	−0.042
48	2s^{2}2p^{5}4d	(3/2,3/2)$_3$	0.999	168.284		
49	2s^{2}2p^{5}4d	(3/2,3/2)$_2$	0.814	168.310		
50	2s^{2}2p^{5}4d	(3/2,5/2)$_4$	1.000	168.314		
51	2s^{2}2p^{5}4d	(3/2,5/2)$_2$	0.814	168.388		
52	2s^{2}2p^{5}4d	(3/2,5/2)$_3$	0.999	168.473		
53	2s^{2}2p^{5}4s	(1/2,1/2)$_0$	0.997	168.493		
54	2s^{2}2p^{5}4s	(1/2,1/2)$_1$	0.961	168.510	168.376	−0.080
55	2s^{2}2p^{5}4d	(3/2,5/2)$_1$	0.890	168.844	168.738	−0.063
56	2s^{2}2p^{5}4f	(3/2,5/2)$_1$	0.999	169.319		
57	2s^{2}2p^{5}4f	(3/2,5/2)$_4$	0.994	169.350		
58	2s^{2}2p^{5}4f	(3/2,5/2)$_2$	0.733	169.359		
59	2s^{2}2p^{5}4f	(3/2,7/2)$_5$	1.000	169.377		
60	2s^{2}2p^{5}4f	(3/2,7/2)$_3$	0.884	169.414		
61	2s^{2}2p^{5}4f	(3/2,7/2)$_2$	0.733	169.425		
62	2s^{2}2p^{5}4f	(3/2,7/2)$_3$	0.884	169.434		

Table 1. (Continued.)

No.	Conf.	Level (j–j)	Purity	MCDF[a] energy	Exp.[b] energy	% Diff.
63	$2s^22p^54f$	$(3/2,7/2)_4$	0.994	169.460		
64	$2s^22p^54p$	$(1/2,1/2)_1$	0.999	170.087		
65	$2s^22p^54p$	$(1/2,3/2)_1$	0.999	170.499		
66	$2s^22p^54p$	$(1/2,1/2)_0$	0.993	170.530		
67	$2s^22p^54p$	$(1/2,3/2)_2$	1.000	170.534		
68	$2s^22p^54d$	$(1/2,3/2)_2$	1.000	172.392		
69	$2s^22p^54d$	$(1/2,5/2)_2$	0.999	172.486		
70	$2s^22p^54d$	$(1/2,5/2)_3$	1.000	172.530		
71	$2s^22p^54d$	$(1/2,3/2)_1$	0.996	172.690	172.621	−0.040
72	$2s^22p^54f$	$(1/2,1/2)_3$	1.000	173.506		
73	$2s^22p^54f$	$(1/2,5/2)_2$	1.000	173.531		
74	$2s^22p^54f$	$(1/2,7/2)_4$	1.000	173.548		
75	$2s^22p^54f$	$(1/2,7/2)_3$	0.999	173.551		
76	$2s2p^64s$	$(1/2,1/2)_1$	0.995	181.982		
77	$2s2p^64s$	$(1/2,1/2)_0$	0.999	182.268		
78	$2s^22p^55s$	$(3/2,1/2)_2$	0.978	183.313		
79	$2s^22p^55s$	$(3/2,1/2)_1$	0.933	183.337	183.258	−0.043
80	$2s2p^64p$	$(1/2,1/2)_0$	0.998	183.598		
81	$2s2p^64p$	$(1/2,1/2)_1$	0.925	183.675	183.420	−0.139
82	$2s2p^64p$	$(1/2,3/2)_2$	0.977	184.048		
83	$2s2p^64p$	$(1/2,3/2)_1$	0.991	184.082	183.779	−0.165
84	$2s^22p^55p$	$(3/2,1/2)_1$	0.983	184.146		
85	$2s^22p^55p$	$(3/2,1/2)_2$	0.998	184.155		
86	$2s^22p^55p$	$(3/2,3/2)_3$	0.998	184.334		
87	$2s^22p^55p$	$(3/2,3/2)_1$	0.984	184.356		
88	$2s^22p^55p$	$(3/2,3/2)_2$	0.999	184.395		
89	$2s^22p^55p$	$(3/2,3/2)_0$	0.997	184.662		
90	$2s^22p^55d$	$(3/2,3/2)_0$	0.999	185.212		
91	$2s^22p^55d$	$(3/2,3/2)_1$	0.930	185.246		
92	$2s^22p^55d$	$(3/2,3/2)_3$	0.999	185.283		
93	$2s^22p^55d$	$(3/2,3/2)_2$	0.871	185.299		
94	$2s^22p^55d$	$(3/2,5/2)_4$	1.000	185.301		
95	$2s^22p^55d$	$(3/2,5/2)_2$	0.871	185.336		
96	$2s^22p^55d$	$(3/2,5/2)_3$	0.999	185.376		
97	$2s^22p^55d$	$(3/2,5/2)_1$	0.928	185.554	185.508	−0.025
98	$2s^22p^55f$	$(3/2,5/2)_1$	0.791	185.679		
99	$2s^22p^55f$	$(3/2,5/2)_2$	0.604	185.723		
100	$2s^22p^55f$	$(3/2,7/2)_3$	0.811	185.792		
101	$2s^22p^55f$	$(3/2,5/2)_4$	0.996	185.812		
102	$2s^22p^55f$	$(3/2,7/2)_5$	1.000	185.825		
103	$2s^22p^55g$	$(3/2,7/2)_2$	0.979	185.839		
104	$2s^22p^55f$	$(3/2,7/2)_2$	0.738	185.847		
105	$2s^22p^55f$	$(3/2,5/2)_3$	0.936	185.848		
106	$2s^22p^55g$	$(3/2,9/2)_3$	0.926	185.852		
107	$2s^22p^55f$	$(3/2,7/2)_4$	0.996	185.866		
108	$2s^22p^55g$	$(3/2,7/2)_3$	0.935	185.888		
109	$2s^22p^55g$	$(3/2,7/2)_5$	0.994	185.894		
110	$2s^22p^55g$	$(3/2,9/2)_4$	0.927	185.897		
111	$2s^22p^55g$	$(3/2,9/2)_6$	1.000	185.904		
112	$2s^22p^55g$	$(3/2,7/2)_4$	0.936	185.914		
113	$2s^22p^55g$	$(3/2,9/2)_5$	0.994	185.925		
114	$2s2p^64d$	$(1/2,3/2)_1$	0.790	185.980		
115	$2s2p^64d$	$(1/2,3/2)_2$	0.763	185.986		
116	$2s2p^64d$	$(1/2,5/2)_3$	0.871	186.021		
117	$2s2p^64d$	$(1/2,5/2)_2$	0.877	186.172		
118	$2s2p^64f$	$(1/2,5/2)_3$	0.983	186.970		
119	$2s2p^64f$	$(1/2,5/2)_2$	0.979	186.994		
120	$2s2p^64f$	$(1/2,7/2)_4$	0.989	186.995		
121	$2s2p^64f$	$(1/2,7/2)_3$	0.976	187.045		
122	$2s^22p^55s$	$(1/2,1/2)_0$	0.999	187.486		
123	$2s^22p^55s$	$(1/2,1/2)_1$	0.999	187.504		

Table 1. (Continued.)

No.	Conf.	Level (j–j)	Purity	MCDF[a] energy	Exp.[b] energy	% Diff.
124	$2s^2 2p^5 5p$	$(1/2, 1/2)_1$	0.999	188.283		
125	$2s^2 2p^5 5p$	$(1/2, 1/2)_0$	0.998	188.475		
126	$2s^2 2p^5 5p$	$(1/2, 3/2)_1$	1.000	188.489		
127	$2s^2 2p^5 5p$	$(1/2, 3/2)_2$	0.999	188.505		
128	$2s^2 2p^5 5d$	$(1/2, 3/2)_2$	1.000	189.406		
129	$2s^2 2p^5 5d$	$(1/2, 5/2)_2$	1.000	189.457		
130	$2s^2 2p^5 5d$	$(1/2, 5/2)_3$	1.000	189.476		
131	$2s^2 2p^5 5d$	$(1/2, 3/2)_1$	0.999	189.547	189.492	−0.020
132	$2s^2 2p^5 5f$	$(1/2, 5/2)_3$	0.999	189.957		
133	$2s^2 2p^5 5f$	$(1/2, 5/2)_2$	1.000	189.974		
134	$2s^2 2p^5 5f$	$(1/2, 7/2)_4$	1.000	189.980		
135	$2s^2 2p^5 5f$	$(1/2, 7/2)_3$	0.999	189.982		
136	$2s^2 2p^5 5g$	$(1/2, 7/2)_4$	0.999	190.039		
137	$2s^2 2p^5 5g$	$(1/2, 7/2)_3$	0.998	190.049		
138	$2s^2 2p^5 5g$	$(1/2, 9/2)_5$	1.000	190.051		
139	$2s^2 2p^5 5g$	$(1/2, 9/2)_4$	0.997	190.060		

[a] Present multi-configuration Dirac–Fock calculation.
[b] NIST Atomic Spectroscopic Data:
http://physics.nist.gov/PhysRefData/contents-atomic.html.

Table 2. Weighted length oscillator strengths and ratios of velocity to length oscillator strengths for all electric-dipole transitions to the ground state in Kr^{26+}.

Level no.	Designation	Present gf	vel/ len	gf (Rice *et al*)
3	$2s^2 2p^5 3s$ $(3/2, 1/2)_1$	1.34×10^{-1}	0.98	–
7	$2s^2 2p^5 3s$ $(1/2, 1/2)_1$	8.45×10^{-2}	0.98	–
17	$2s^2 2p^5 3d$ $(3/2, 3/2)_1$	6.41×10^{-3}	0.95	7.79×10^{-3}
23	$2s^2 2p^5 3d$ $(3/2, 5/2)_1$	1.55×10^{0}	0.96	1.54×10^{0}
27	$2s^2 2p^5 3d$ $(1/2, 3/2)_1$	1.93×10^{0}	0.96	1.94×10^{0}
31	$2s 2p^6 3p$ $(1/2, 1/2)_1$	8.97×10^{-2}	1.00	8.75×10^{-2}
33	$2s 2p^6 3p$ $(1/2, 3/2)_1$	3.05×10^{-1}	1.00	3.05×10^{-1}
39	$2s^2 2p^5 4s$ $(3/2, 1/2)_1$	2.48×10^{-2}	0.91	2.47×10^{-2}
47	$2s^2 2p^5 4d$ $(3/2, 3/2)_1$	3.26×10^{-3}	0.93	–
54	$2s^2 2p^5 4s$ $(1/2, 1/2)_1$	7.94×10^{-2}	0.93	6.80×10^{-2}
55	$2s^2 2p^5 4d$ $(3/2, 5/2)_1$	4.29×10^{-1}	0.94	4.34×10^{-1}
71	$2s^2 2p^5 4d$ $(1/2, 3/2)_1$	3.38×10^{-1}	0.94	3.30×10^{-1}
79	$2s^2 2p^5 5s$ $(3/2, 1/2)_1$	2.97×10^{-2}	0.82	3.33×10^{-2}
81	$2s 2p^6 4p$ $(1/2, 1/2)_1$	1.77×10^{-2}	1.00	1.30×10^{-2}
83	$2s 2p^6 4p$ $(1/2, 3/2)_1$	1.20×10^{-1}	0.95	1.17×10^{-1}
91	$2s^2 2p^5 5d$ $(3/2, 3/2)_1$	4.98×10^{-4}	0.90	–
97	$2s^2 2p^5 5d$ $(3/2, 5/2)_1$	2.24×10^{-1}	0.91	2.33×10^{-1}
123	$2s^2 2p^5 5s$ $(1/2, 1/2)_1$	2.50×10^{-3}	0.62	–
131	$2s^2 2p^5 5d$ $(1/2, 3/2)_1$	1.31×10^{-1}	0.91	1.37×10^{-1}

suite of programs [23–25]. In order to combine these two sets of programs, the Hamiltonian matrix elements generated by the inner-region DARC codes for a given $J\Pi$ symmetry were reformatted to be consistent with those in the BP suite of codes [26, 27]. They may be run with or without radiation damping. A flow diagram for calculations that include damping is shown in a paper on electron-impact excitation of W^{46+} [20]. The CC expansion for the scattering calculations included all 139 levels listed in table 1. The size of the R-matrix 'box' was 3.6 au and we employed 33 basis orbitals to represent the $(N+1)$-electron continuum per angular momentum. All partial waves from $J = 1/2$ to 71/2 were included explicitly and contributions

from higher partial waves were estimated using a top-up procedure [28].

Below the highest excitation threshold, a very fine energy mesh must be implemented in order to resolve the majority of narrow resonances. For this reason, for all partial waves from $J = 1/2$ to 21/2, we first performed a calculation with 80 000 points in the energy range from the first threshold to just above the highest threshold. We then doubled the number of mesh points to 160 000. By comparing effective collision strengths from these two calculations, we were able to confirm that most resonances were resolved. Our final 160 000 points calculation employed an energy-mesh spacing of 4.36×10^{-4} Ry. An additional 200 energy mesh points for these lower partial waves were used to span the energy range from just above the highest threshold to a maximum energy of 570 Ry. For the higher partial waves from $J = 23/2$ to 71/2, we calculated 2000 mesh points to cover the energy range from the first threshold to 570 Ry.

In table 4, we compare cross sections from the present calculation with those from the earlier 27-level BP R-matrix calculation of Gupta *et al* [13] and the relativistic DW calculation of Reed [11]. The cross sections from these two prior calculations were determined from collision strengths that are given at energies of 150 Ry, 300 Ry and 500 Ry in [13]. Since no resonances are included in the relativistic DW calculation and only those resonant states attached to the $2p^5 3l$ configurations are included in the BP R-matrix calculation, such comparisons are not meaningful for energies below the highest excitation threshold in the present calculation. Thus, only the values at 300 Ry and 500 Ry were employed here. The cross sections from the present calculation are higher than those from either the BP R-matrix or the relativistic DW calculations for the vast majority of transitions, especially at an energy of 500 Ry. At 300 Ry, the average difference between the present results and those of Gupta *et al* [13] is 8.5%, while the average difference between the present results and those of

Table 3. Diagnostic radiative transitions to the ground level in Kr^{26+} with theoretical and experimental wavelengths and theoretical radiative rates.

Upper level	Transition	Label	Th. λ (Å)	Exp. λ (Å)	MCDF A (s^{-1})
$2p^5 3s\ (3/2,1/2)_2$	$(2 \rightarrow 1)$	M2	7.5191	7.5184	5.40×10^6
$2p^5 3s\ (3/2,1/2)_1$	$(3 \rightarrow 1)$	3G	7.5047	7.5038	5.27×10^{12}
$2p^5 3s\ (1/2,1/2)_1$	$(7 \rightarrow 1)$	3F	7.2651	7.2669	3.56×10^{12}
$2p^5 3d\ (3/2,3/2)_1$	$(17 \rightarrow 1)$	3E	6.9596	6.9591	2.94×10^{11}
$2p^5 3d\ (3/2,5/2)_1$	$(23 \rightarrow 1)$	3D	6.8748	6.8787	7.30×10^{13}
$2p^5 3d\ (1/2,3/2)_1$	$(27 \rightarrow 1)$	3C	6.6893	6.6973	9.60×10^{13}

Table 4. Cross sections in units of cm^2 for excitations from the $2p^6\ ^1S_0$ ground level to the first 26 excited levels in Kr^{26+} at excitation energies of 300 Ry and 500 Ry. The numbers in parentheses denote powers of 10.

Upper level	300 Ry			500 Ry		
	BPRM[a]	Rel DW[b]	Pres RM[c]	BPRM[a]	Rel DW[b]	Pres RM[c]
$2p^5 3s\ (3/2,1/2)_2$	8.94(−23)	8.80(−23)	9.98(−23)	2.08(−23)	2.05(−23)	2.73(−23)
$2p^5 3s\ (3/2,1/2)_1$	5.22(−22)	6.63(−22)	7.29(−22)	4.87(−22)	5.43(−22)	7.04(−22)
$2p^5 3p\ (3/2,1/2)_1$	1.60(−22)	1.73(−22)	1.85(−22)	3.87(−23)	4.11(−23)	5.26(−23)
$2p^5 3p\ (3/2,1/2)_2$	4.25(−22)	4.72(−22)	4.88(−22)	2.92(−22)	2.52(−22)	3.14(−22)
$2p^5 3s\ (1/2,1/2)_0$	1.90(−23)	1.76(−23)	2.01(−23)	4.37(−24)	4.40(−24)	5.53(−24)
$2p^5 3s\ (1/2,1/2)_1$	2.99(−22)	4.16(−22)	4.52(−22)	2.60(−22)	3.18(−22)	4.24(−22)
$2p^5 3p\ (3/2,3/2)_3$	2.30(−22)	2.20(−22)	2.34(−22)	5.22(−23)	4.84(−23)	6.21(−23)
$2p^5 3p\ (3/2,3/2)_1$	1.10(−22)	1.06(−22)	1.20(−22)	2.61(−23)	2.35(−23)	3.32(−23)
$2p^5 3p\ (3/2,3/2)_2$	3.81(−22)	3.90(−22)	4.17(−22)	2.84(−22)	2.16(−22)	2.80(−22)
$2p^5 3p\ (3/2,3/2)_0$	2.06(−21)	2.05(−21)	2.02(−21)	9.69(−22)	1.08(−21)	1.29(−21)
$2p^5 3p\ (1/2,1/2)_1$	9.44(−23)	9.09(−23)	1.01(−22)	2.14(−23)	2.05(−23)	2.69(−23)
$2p^5 3p\ (1/2,3/2)_1$	1.11(−22)	1.11(−22)	1.21(−22)	2.60(−23)	2.49(−23)	3.30(−23)
$2p^5 3p\ (1/2,3/2)_2$	3.81(−22)	4.31(−22)	4.41(−22)	2.51(−22)	2.32(−22)	2.84(−22)
$2p^5 3d\ (3/2,3/2)_0$	9.85(−23)	9.97(−23)	1.04(−22)	2.04(−23)	2.05(−23)	2.58(−23)
$2p^5 3p\ (1/2,1/2)_0$	5.48(−21)	5.40(−21)	5.08(−21)	3.27(−21)	2.83(−21)	3.27(−21)
$2p^5 3d\ (3/2,3/2)_1$	3.08(−22)	3.11(−22)	3.34(−22)	9.15(−23)	9.09(−23)	1.20(−22)
$2p^5 3d\ (3/2,3/2)_3$	4.75(−22)	4.66(−22)	4.78(−22)	2.39(−22)	2.26(−22)	2.76(−22)
$2p^5 3d\ (3/2,5/2)_2$	2.92(−22)	2.90(−22)	3.00(−22)	5.86(−23)	5.72(−23)	7.17(−23)
$2p^5 3d\ (3/2,5/2)_4$	3.11(−22)	2.99(−22)	3.17(−22)	6.00(−23)	5.72(−23)	7.28(−23)
$2p^5 3d\ (3/2,3/2)_2$	1.33(−22)	1.26(−22)	1.42(−22)	2.42(−23)	2.20(−23)	3.15(−23)
$2p^5 3d\ (3/2,5/2)_3$	3.67(−22)	3.61(−22)	3.62(−22)	2.02(−22)	1.88(−22)	2.29(−22)
$2p^5 3d (3/2,5/2)_1$	1.30(−20)	1.46(−20)	1.45(−20)	9.74(−21)	9.93(−21)	1.20(−20)
$2p^5 3d\ (1/2,3/2)_2$	1.55(−22)	1.47(−22)	1.58(−22)	2.89(−23)	2.79(−23)	3.58(−23)
$2p^5 3d\ (1/2,5/2)_2$	2.44(−22)	2.32(−22)	2.44(−22)	4.77(−23)	4.55(−23)	5.74(−23)
$2p^5 3d\ (1/2,5/2)_3$	4.40(−22)	4.25(−22)	4.31(−22)	2.26(−22)	2.11(−22)	2.58(−22)
$2p^5 3d\ (1/2,3/2)_1$	1.64(−20)	1.46(−20)	1.72(−20)	1.21(−20)	1.19(−20)	1.40(−20)

[a] Determined from the 27-level BP *R*-matrix collisions strengths of Gupta *et al* [13].
[b] Determined from the relativistic DW collisions strengths of Reed [11] given in [13].
[c] From the present 139-level Dirac *R*-matrix calculation.

Reed [11] is 6.2%. At 500 Ry, these average differences have increased to 20.8% and 23.8%, respectively.

Some of these differences are due to the different target states used in each calculation. For example, the energies in the present calculation are in better agreement with experiment than those from the BP structure calculations of Gupta *et al* [13]. However, the fact that the present cross sections are in general higher, and these differences increase substantially with energy strongly suggests that they are due primarily to a lack of completeness in the partial-wave sums used in the earlier calculations. The sum used by Gupta *et al* [13] only included partial waves up through $J = 17/2$; they then topped up their dipole-allowed transitions using a procedure similar to ours. This expansion is not sufficiently complete to achieve convergence, especially at energies as high as 500 Ry. A

description of the partial-wave sum employed in the relativistic DW calculation is not available.

In figure 1, we show excitation cross sections from the ground level to the four levels arising from the $2s^2 2p^5 3s$ configuration. The dotted curves with the complex resonance structures are from the calculation with damping. In order to show the effects of radiation damping on these cross sections, we also calculated the excitation cross sections for these four transitions convoluted with a 2.94 Ry (40 eV) Gaussian and compared the results with (solid curves) and without (the long dashed curves) damping. As can be seen, the cross sections are quite close and a calculation without damping would be sufficiently accurate, at least for these selected excitations.
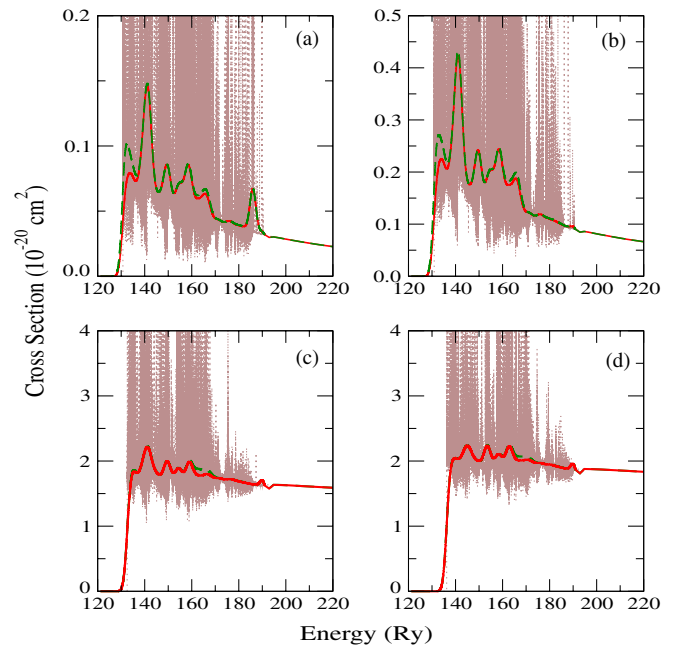
The most pronounced feature for all four of these cross sections is the very large contributions from resonances
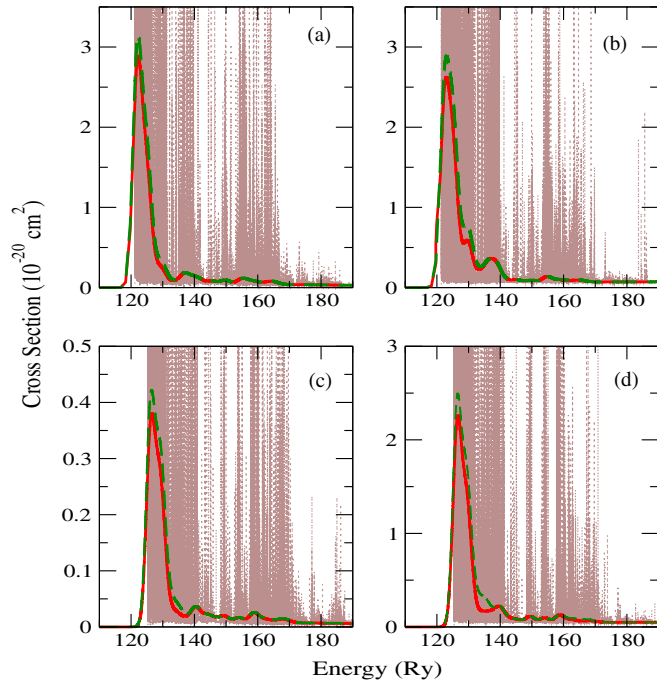
Figure 1. Electron-impact excitation cross sections for transitions from the $2s^2 2p^6\ ^1S$ ground level to the levels of the $2s^2 2p^5 3s$ configuration: (a) to $(3/2,1/2)_2$ (level 2); (b) to $(3/2,1/2)_1$ (level 3); (c) to $(1/2,1/2)_0$ (level 6) and (d) to $(1/2,1/2)_1$ (level 7). The dotted curves with the pronounced resonance structures are from the 139-level *R*-matrix calculation with radiation damping; the smooth solid curves are the cross sections from the 139-level calculation with damping convoluted with a 2.94 Ry Gausssian; and the long dashed curves are the cross sections from the 139-level calculation with no radiative damping convoluted with a 2.94 Ry Gausssian.

Figure 2. Electron-impact excitation cross sections for transitions from the $2s^2 2p^6\ ^1S_0$ ground level to four levels of the $2s^2 2p^5 3d$ configuration: (a) to $(3/2,3/2)_0$ (level 15); (b) to $(3/2,3/2)_1$ (level 17); (c) to $(3/2,5/2)_1$ (level 23); (d) to $(1/2,3/2)_1$ (level 27). The dotted curves with the pronounced resonance structures are from the 139-level *R*-matrix calculation with radiation damping; the smooth solid curves are the cross sections from the 139-level calculation with damping convoluted with a 2.94 Ry Gausssian; and the long dashed curves are the cross sections from the 139-level calculation with no radiative damping convoluted with a 2.94 Ry Gausssian.

at low energy. Clearly, a DW calculation that does not include perturbative calculations of resonant recombination followed by autoionization would be completely inaccurate. Furthermore, it is clear that the resonant contributions above the highest $2p^5 3d$ level at approximately 136 Ry are smaller than those at lower energy; however, they are far from negligible. In addition, some of the contributions below this energy arise from resonances attached to levels above the highest $2p^5 3d$ level. Thus the 27-level BP *R*-matrix results of Gupta *et al* [13] will have noticeably smaller resonance contributions for excitation to the $2p^5 3s$ levels than the cross sections shown here.

In figure 2, we show similar curves for excitation from the ground level to four of the twelve levels arising from the $2s^2 2p^5 3d$ configuration. By comparing the convoluted cross sections, we see that the effects of radiation damping are again very small. Furthermore, the resonance contributions for the non-dipole excitation to the $2s^2 2p^5 3d\ (3/2,3/2)_0$ level and the weak dipole excitation to the $2s^2 2p^5 3d\ (3/2,3/2)_1$ level are quite important and they are dominated by resonances attached to levels above the highest level of the $2s^2 2p^5 3d$ configuration. However, as one would expect, the effects of resonances on the cross sections for the strong dipole excitations to the $2s^2 2p^5 3d\ (3/2,5/2)_1$ and the $2s^2 2p^5 3d\ (1/2,3/2)_1$ levels are far less important.

In table 5, we present effective collision strengths calculated both with and without damping for excitation from the ground level to the first 26 excited levels over six temperatures from 5×10^6 K to 3×10^7 K. As can be seen, the effects of damping are again relatively small for these 26 transitions with only three exceeding 10%. When averaged over all 9591 transitions between the 139 levels and over ten temperatures from 5×10^6 K to 5×10^7 K, the average difference between the effective collision strengths with and without damping was only 1.58%. The effective collision strengths, with radiation damping, along with electric-dipole, electric-quadrupole and magnetic-dipole radiative rates are now available at the Oak Ridge National Laboratory (ORNL) Controlled Fusion Atomic Data Center (CFADC) website, at http://www-cfadc.phy.ornl.gov/data_and_codes/home.html.

Finally, we have performed collisional-radiative modeling calculations that utilize the present radiative rates and collisional rates with radiation damping to calculate intensity line ratios involving the six transitions given in table 3. If one assumes that the main population mechanism of any excited level is direct excitation from the ground level (g), then the intensity line ratio for the transition $i \rightarrow g$ to the transition $j \rightarrow g$ is given by

$$\frac{I_{i \rightarrow g}}{I_{j \rightarrow g}} = \frac{Q_{g \rightarrow i}}{Q_{g \rightarrow j}} \frac{B_{i \rightarrow g}}{B_{j \rightarrow g}}. \tag{1}$$

Table 5. Effective collision strengths for excitations from the $2p^6\ ^1S_0$ ground level to the first 26 excited levels in Kr^{26+}. For each transition, the first row is from the *R*-matrix calculation without damping while the second row is from the calculation with damping. The last column lists the percentage differences between these two calculations averaged over the six temperatures. The numbers in parentheses denote powers of 10.

Upper level	Electron temperature (K)						
	5×10^6	7×10^6	9×10^6	1×10^7	2×10^7	3×10^7	Avg. % diff.
$2p^53s\ (3/2,1/2)_2$	8.29(−3)	6.28(−3)	5.09(−3)	4.66(−3)	2.61(−3)	1.85(−3)	
	7.44(−3)	5.65(−3)	4.60(−3)	4.21(−3)	2.37(−3)	1.69(−3)	6.0
$2p^53s\ (3/2,1/2)_1$	9.36(−3)	7.39(−3)	6.27(−3)	5.88(−3)	4.28(−3)	4.00(−3)	
	8.14(−3)	6.48(−3)	5.54(−3)	5.21(−3)	3.94(−3)	3.76(−3)	7.4
$2p^53p\ (3/2,1/2)_1$	3.49(−3)	2.91(−3)	2.54(−3)	2.39(−3)	1.61(−3)	1.26(−3)	
	3.03(−3)	2.58(−3)	2.27(−3)	2.15(−3)	1.48(−3)	1.17(−3)	6.9
$2p^53p\ (3/2,1/2)_2$	4.30(−3)	3.69(−3)	3.31(−3)	3.17(−3)	2.50(−3)	2.26(−3)	
	3.85(−3)	3.36(−3)	3.05(−3)	2.93(−3)	2.37(−3)	2.17(−3)	5.2
$2p^53s\ (1/2,1/2)_0$	1.32(−3)	1.01(−3)	8.27(−4)	7.60(−4)	4.33(−4)	3.11(−4)	
	1.14(−3)	8.80(−4)	7.22(−4)	6.65(−4)	3.84(−4)	2.78(−4)	7.9
$2p^53s\ (1/2,1/2)_1$	7.69(−3)	5.99(−3)	5.02(−3)	4.68(−3)	3.20(−3)	2.84(−3)	
	6.54(−3)	5.14(−3)	4.33(−3)	4.05(−3)	2.88(−3)	2.62(−3)	8.7
$2p^53p\ (3/2,3/2)_3$	4.03(−3)	3.45(−3)	3.05(−3)	2.89(−3)	1.98(−3)	1.56(−3)	
	3.85(−3)	3.31(−3)	2.94(−3)	2.79(−3)	1.93(−3)	1.52(−3)	2.3
$2p^53p\ (3/2,3/2)_1$	3.14(−3)	2.58(−3)	2.21(−3)	2.07(−3)	1.33(−3)	1.01(−3)	
	2.20(−3)	1.88(−3)	1.66(−3)	1.57(−3)	1.07(−3)	8.37(−4)	17.5
$2p^53p\ (3/2,3/2)_2$	3.36(−3)	2.94(−3)	2.67(−3)	2.57(−3)	2.07(−3)	1.90(−3)	
	3.12(−3)	2.76(−3)	2.53(−3)	2.44(−3)	2.00(−3)	1.85(−3)	3.5
$2p^53p\ (3/2,3/2)_0$	8.67(−3)	8.19(−3)	7.90(−3)	7.80(−3)	7.36(−3)	7.26(−3)	
	7.52(−3)	7.34(−3)	7.23(−3)	7.19(−3)	7.04(−3)	7.05(−3)	6.0
$2p^53p\ (1/2,1/2)_1$	2.69(−3)	2.18(−3)	1.86(−3)	1.74(−3)	1.11(−3)	8.41(−4)	
	1.76(−3)	1.50(−3)	1.32(−3)	1.25(−3)	8.54(−4)	6.71(−4)	20.8
$2p^53p\ (1/2,3/2)_1$	2.80(−3)	2.33(−3)	2.02(−3)	1.90(−3)	1.25(−3)	9.57(−4)	
	2.20(−3)	1.90(−3)	1.68(−3)	1.59(−3)	1.08(−3)	8.47(−4)	11.5
$2p^53p\ (1/2,3/2)_2$	3.27(−3)	2.92(−3)	2.68(−3)	2.60(−3)	2.13(−3)	1.96(−3)	
	2.90(−3)	2.64(−3)	2.46(−3)	2.39(−3)	2.03(−3)	1.89(−3)	5.6
$2p^53d\ (3/2,3/2)_0$	1.24(−3)	1.12(−3)	1.02(−3)	9.80(−4)	7.19(−4)	5.82(−4)	
	1.17(−3)	1.06(−3)	9.79(−4)	9.42(−4)	6.99(−4)	5.68(−4)	2.8
$2p^53p\ (1/2,1/2)_0$	1.71(−2)	1.69(−2)	1.69(−2)	1.69(−2)	1.70(−2)	1.73(−2)	
	1.61(−2)	1.62(−2)	1.63(−2)	1.63(−2)	1.68(−2)	1.71(−2)	2.5
$2p^53d\ (3/2,3/2)_1$	3.45(−3)	3.12(−3)	2.86(−3)	2.75(−3)	2.08(−3)	1.74(−3)	
	3.28(−3)	2.99(−3)	2.75(−3)	2.66(−3)	2.03(−3)	1.70(−3)	2.4
$2p^53d\ (3/2,3/2)_3$	3.80(−3)	3.41(−3)	3.14(−3)	3.03(−3)	2.44(−3)	2.19(−3)	
	3.46(−3)	3.15(−3)	2.93(−3)	2.84(−3)	2.34(−3)	2.12(−3)	4.4
$2p^53d\ (3/2,5/2)_2$	4.13(−3)	3.67(−3)	3.32(−3)	3.18(−3)	2.27(−3)	1.81(−3)	
	3.94(−3)	3.53(−3)	3.21(−3)	3.07(−3)	2.21(−3)	1.77(−3)	2.2
$2p^53d\ (3/2,5/2)_4$	4.48(−03)	3.99(−03)	3.61(−03)	3.45(−03)	2.45(−03)	1.95(−03)	
	4.38(−03)	3.91(−03)	3.54(−03)	3.39(−03)	2.42(−03)	1.93(−03)	1.1
$2p^53d\ (3/2,3/2)_2$	3.08(−03)	2.65(−03)	2.33(−03)	2.21(−03)	1.47(−03)	1.13(−03)	
	2.93(−03)	2.53(−03)	2.24(−03)	2.12(−03)	1.43(−03)	1.10(−03)	2.5
$2p^53d\ (3/2,5/2)_3$	3.20(−03)	2.85(−03)	2.60(−03)	2.50(−03)	1.97(−03)	1.76(−03)	
	3.11(−03)	2.78(−03)	2.54(−03)	2.44(−03)	1.94(−03)	1.74(−03)	1.5
$2p^53d(3/2,5/2)_1$	3.37(−02)	3.51(−02)	3.65(−02)	3.72(−02)	4.37(−02)	4.93(−02)	
	3.35(−02)	3.49(−02)	3.63(−02)	3.70(−02)	4.36(−02)	4.92(−02)	0.3
$2p^53d\ (1/2,3/2)_2$	2.41(−03)	2.12(−03)	1.91(−03)	1.82(−03)	1.27(−03)	1.00(−03)	
	2.33(−03)	2.06(−03)	1.86(−03)	1.77(−03)	1.25(−03)	9.85(−04)	1.7
$2p^53d\ (1/2,5/2)_2$	3.61(−03)	3.20(−03)	2.88(−03)	2.75(−03)	1.93(−03)	1.53(−03)	
	3.49(−03)	3.10(−03)	2.80(−03)	2.67(−03)	1.89(−03)	1.50(−03)	1.8
$2p^53d\ (1/2,5/2)_3$	3.12(−03)	2.83(−03)	2.62(−03)	2.54(−03)	2.09(−03)	1.91(−03)	
	3.05(−03)	2.77(−03)	2.58(−03)	2.50(−03)	2.07(−03)	1.89(−03)	1.1
$2p^53d\ (1/2,3/2)_1$	3.83(−02)	4.01(−02)	4.19(−02)	4.28(−02)	5.08(−02)	5.76(−02)	
	3.82(−02)	4.00(−02)	4.18(−02)	4.27(−02)	5.07(−02)	5.75(−02)	0.1

The Maxwellian excitation rate coefficient from the ground level to level i is given by

$$Q_{g\to i} = \int_0^\infty \sigma_{g\to i}(E) v f(E)\, dE, \qquad (2)$$

where $\sigma_{g\to i}$ is the excitation cross section, v is the free-electron velocity and $f(E)$ is the Maxwellian energy distribution. $B_{i\to g}$ is the branching ratio from level i to the ground level versus radiation to all lower levels
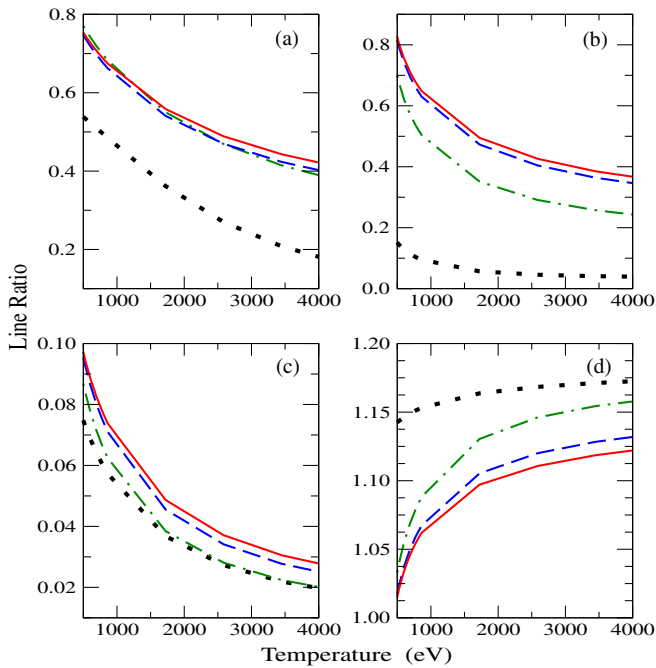
Figure 3. Line-intensity ratios as a function of temperature for various transitions in Kr^{26+} determined from the 139-level *R*-matrix calculation with radiation damping: (a) the M2/3G line ratio; (b) the 3E/3C line ratio; (c) the 3F/3C line ratio and (d) the 3C/3D line ratio. All collisional radiative calculations were performed at an electron density of 1.0×10^{14} cm^{-3}. The dotted curves are calculated from equation (1) and are essentially the ratios of Maxwellian rate coefficients; the dot-dashed curves are from collisional radiative modeling that includes all levels through $2s^2 2p^5 3l$ (lowest 27 levels in table 1); the long dashed curves are from collisional radiative modeling that includes all levels through $2s^2 2p^5 4l$ (the lowest 75 levels in table 1); the solid curves are from collisional radiative modeling that includes all 139 levels in table 1.

$$B_{i \to g} = \frac{A_{i \to g}}{\sum_{k < i} A_{i \to k}}, \qquad (3)$$

where $A_{i \to k}$ is the radiative rate from level *i* to a lower level *k*. For the six transitions given in table 3, the radiative branching ratios to the ground level are 1.00, with the exception of transition E which has a branching ratio of 0.92. Thus, the line ratios in this simple approximation are essentially equal to the ratios of the Maxwellian excitation rate coefficients.

However, equation (1) is not adequate for most cases and one must perform collisional-radiative modeling calculations to first determine the population number densities for each level as a function of density and temperature. The intensity line ratios are then given by

$$\frac{I_{i \to g}}{I_{j \to g}} = \frac{N_i}{N_j} \frac{A_{i \to g}}{A_{j \to g}}, \qquad (4)$$

where N_i is the population number density of level *i* and $A_{i \to g}$ is the radiative rate from level *i* to the ground level. In the collisional-radiative calculations presented here, we employed the isolated-ion approximation so that the population for a given level depends only on radiative decays from that level, radiative cascades from all higher levels, collisional excitation and de-excitation from all other levels to that level, and collisional excitation and de-excitation from that level to all

other levels. A more complete model would also include the influence of ionization and recombination between adjacent ions.

Line ratios involving the six transitions listed in table 3 as a function of temperature are presented in figure 3. They are all calculated at an electron density of 1.0×10^{14} cm^{-3}. We show results determined from equation (1) (dotted curves) and when we included only the lowest 27 levels (dashed-dot curves), the lowest 75 levels (dashed curves) and all 139 levels (solid curves) in the collisional radiative modeling.

We found that these ratios do not change appreciably as a function of density for densities less than approximately 1.0×10^{15} cm^{-3}. Therefore, they cannot be used as density diagnostics for the range of densities present in tokamak plasmas. For the results shown here at a density of 1.0×10^{14} cm^{-3}, the level populations thus depend almost entirely on radiative cascades and very little on collisional excitation and de-excitation. As we see from figure 3, the ratios M2/3G, 3E/3C and 3F/3C should be effective as temperature diagnostics, while variations with temperature for the 3C/3D line ratio are probably too small for this purpose.

By comparing the dotted curve with the other three curves for the M2/3G ratio shown in (a), it is clear that radiative cascades from the $2s^2 2p^5 3l$ levels have a pronounced effect on this particular line ratio, but the effects of cascades from still higher levels are not significant. In the case of the 3E/3C ratio shown in (b), the radiative cascades included in the 27-level modeling calculation again have a large effect, but now the additional cascades included in the 75-level calculation are also significant, while the effects of cascades from still higher levels are small. This is also true of the 3C/3D ratio shown in (d), especially at the lower temperatures. Finally, the effects of cascades from the $2s^2 2p^5 3l$ levels on the 3F/3C ratio shown in (c) are small, especially at lower temperatures; however, those from higher levels are more significant. Some additional changes in these ratios would have occurred if we had included levels above the highest level of $2s^2 2p^5 5l$ configuration; however, these curves indicate that they would be relatively small.

4. Conclusions

We have completed the first *R*-matrix calculation on neon-like Kr^{26+} that includes levels above the highest level of the $2s^2 2p^5 3l$ configuration. The effects of radiation damping on the resonance contributions to excitation in this ion were investigated and found to be small. All electric dipole, electric quadrupole, magnetic dipole radiative rates and effective collision strengths between all 139 levels have been generated and these data are available on the ORNL CFADC website.

Simplified collisional-radiative modeling on this ion was carried out and intensity line ratios were calculated involving six different transitions used previously in other Ne-like systems. For the range of densities important in tokamak plasmas, these line ratios do not vary with density. However, the effects of radiative cascades on these line ratios are significant and collisional-radiative modeling is required to obtain accurate values.

Acknowledgments

References

[1] Smith B W, Raymond J C, Mann J B and Cowan R D 1985 *Astrophys. J.* **298** 898
[2] Doron R and Behar E 2002 *Astrophys. J.* **574** 518
[3] Gu M F 2003 *Astrophys. J.* **582** 1241
[4] Chen G X 2008 *Phys. Rev.* A **77** 022701
[5] Chen G X and Pradhan A K 2002 *Phys. Rev. Lett.* **89** 013202
[6] Chen G X and Pradhan A K 2003 *J. Phys. B: At. Mol. Opt. Phys.* **36** 453
[7] Loch S D, Pindzola M S, Ballance C P and Griffin D C 2006 *J. Phys. B: At. Mol. Opt. Phys.* **39** 85
[8] Chen G X 2007 *Phys. Rev.* A **76** 062708
[9] Rice J E, Fournier K B, Goetz J A, Marmar E S and Terry J L 2000 *J. Phys. B: At. Mol. Opt. Phys.* **33** 5435
[10] Bhatia A K, Feldman U and Seely J F 1985 *At. Data Nucl. Data Tables* **32** 435
[11] Reed K J 1985 Internal Memo, Lawrence Livermore National Laboratory
[12] Zhang H, Sampson D H, Clark R E H and Mann J B 1987 *At. Data Nucl. Data Tables* **37** 17
[13] Gupta G P, Deb N C and Msezane A Z 2000 *Phys. Scr.* **61** 175
[14] Dyall K G, Grant I P, Johnson C T, Parpia F A and Plummer E P 1989 *Comput. Phys. Commun.* **55** 425
[15] Parpia F A, Froese Fischer C and Grant I P 1996 *Comput. Phys. Commun.* **94** 249
[16] Dong C Z, Xie L Y, Fritzsche S and Kato T 2003 *Nucl. Instrum. Methods Phys. Res.* B **205** 87
[17] Berengut J C, Dzuba V A, Flambaum V V and Marchenko M V 2004 *Phys. Rev.* A **70** 064101
[18] Berengut J C, Flambaum V V and Kozlov M G 2005 *Phys. Rev.* A **72** 044501
[19] Berengut J C, Flambaum V V and Kozlov M G 2006 *Phys. Rev.* A **73** 012504
[20] Ballance C P and Griffin D C 2006 *J. Phys. B: At. Mol. Opt. Phys.* **39** 3617
[21] Norrington P H and Grant I P 1987 *J. Phys. B: At. Mol. Opt. Phys.* **20** 4869
[22] Ait-Tahar S, Grant I P and Norrington N H 1996 *Phys. Rev.* A **54** 3984
[23] Ballance C P and Griffin D C 2004 *J. Phys. B: At. Mol. Opt. Phys.* **37** 2943
[24] Mitnik D M, Griffin D C and Badnell N R 2001 *J. Phys. B: At. Mol. Opt. Phys.* **34** 4455
[25] Mitnik D M, Griffin D C, Ballance C P and Badnell N R 2003 *J. Phys. B: At. Mol. Opt. Phys.* **36** 717
[26] Badnell N R, Berrington K A, Summers H P, O'Mullane M G, Whiteford A D and Ballance C P 2004 *J. Phys. B: At. Mol. Opt. Phys.* **37** 4589
[27] Berrington K A, Ballance C P, Griffin D C and Badnell N R 2005 *J. Phys. B: At. Mol. Opt. Phys.* **38** 1667
[28] Burgess A 1974 *J. Phys. B: At. Mol. Phys.* **7** L364